

THE VELOCITY AND VORTICITY FIELDS BENEATH GRAVITY-CAPILLARY WAVES EXHIBITING PARASITIC RIPPLES

H. J. Lin and Marc Perlin, *University of Michigan, Ann Arbor, MI 48109-2125, USA, perlin@umich.edu*

I. INTRODUCTION

The dynamical theory of the generation of parasitic capillary waves (ripples) has been developed by Longuet-Higgins,¹ Crapper,² Ruvinsky and Freidman,³ and Ruvinsky, Feldstein, and Freidman.⁴ However, there is another important feature of these short gravity waves with parasitic capillaries (capillary ripples) that has been pointed out by Okuda *et al.*,⁵ and Ebuchi *et al.*⁶ In the crest of steep wind-generated waves, they observed a strong vortical region in the neighborhood of the parasitic capillary ripples. Based on a boundary-layer theory, Longuet-Higgins⁷ argued that the primary source of vorticity in this region, which he called a “capillary roller,” is the parasitic capillary ripples themselves, not the wind. Longuet-Higgins showed that the peak vorticity occurs slightly aft of a capillary ripple’s trough and that a mean flux of vorticity is induced by the capillary waves. Based on arguments of the appearance of strong vortices, he determined that the resulting surface currents that form beneath steep parasitic capillary ripples can approach the phase speed of gravity-capillary waves. Mui and Dommermuth⁸ introduced a numerical algorithm that is capable of imposing more complicated boundary conditions on a curvilinear boundary. They used this algorithm to simulate the flow field/vortical structure of a 50 mm long, near-breaking gravity-capillary wave. Their calculation quantitatively matched Longuet-Higgins’ model except that the strong vortical region in the crest of the underlying wave is absent in the numerical results. More recently, Lin and Rockwell⁹ observed the near-surface flow field beneath a stationary gravity-capillary wave train (with wavelengths of 100 to 200 mm) generated above a hydrofoil in a recirculating free-surface water channel. They used conventional digital PIV to estimate velocity; however, an accurate velocity/vorticity measurement of progressive waves with short wavelengths has never been completed due to the difficulties of investigating small-scale fluid structure within a fairly thin boundary layer.

Progressive gravity-capillary waves with moderate steepness (0.130 through 0.230) are studied, as generated by a flap-type wave maker in a closed water channel. The associated wavelengths are about 50 mm through 100 mm. The steepnesses are chosen such that the parasitic capillary ripples are present but the wave remains quasi-steady and two dimensional. (For larger values, the interactions between the underlying waves and the parasitic capillary ripples become dominant and the flow is not steady, see Perlin *et al.*¹⁰ and Jiang *et al.*¹¹). Because of the relatively short wavelengths and the moderate steepnesses, novel experimental techniques are required. A specially designed V-shaped-bottom water channel and an improved PIV technique, sub-pattern PIV, as discussed in detail by Lin and Perlin,¹² are used for the present study.

II. EXPERIMENTAL TECHNIQUES

The apparatus and techniques used for the velocity measurements and thus the calculation of vorticity beneath gravity-capillary waves are essentially identical to those described in Lin and Perlin;¹² hence, only the rudiments of the specially developed techniques are discussed. A Brewster angle imaging setup with a laser-light control system for recording images is used with a new processing method known as sub-pattern PIV. These new techniques are developed to improve the velocity flow-field measurement capability within a free-surface boundary layer region where progressive gravity-capillary waves are present. Due to the extremely thin but rather vortical characteristics of the free-surface boundary layer of gravity-capillary waves, conventional PIV methods fail to estimate velocity vectors at an acceptable detection rate. This failure is a direct consequence of optimal PIV parameters (e.g. window size, seeding density) that are difficult to achieve for this flow. The new sub-pattern PIV method has similarities with both the super-resolution PIV technique (Keane *et al.*¹³) and the particle image distortion (PID) technique (Huang *et al.*¹⁴). Similar to the PID method, an artificial image distortion is included in sub-pattern PIV; however, unlike PID, conventional PIV is not adopted for the first iteration as it yields invalid estimates for velocity gradients larger than an allowable value. To determine the required image distortion (that essentially removes the velocity gradient effects and thus facilitates use of conventional PIV techniques), appropriate sub-interrogation windows are used. The length/width of these sub-interrogation windows that gives the best results is 1/3 the length of the full-sized interrogation window. Three properly chosen sub-interrogation windows are required to give a first-approximation to the actual distortion between images. A procedure is used to locate the most-concentrated particle image sub-patterns. The three most-concentrated particle image sub-patterns are chosen as long as each represents independent data. By requiring that the sub-interrogation windows not exceed 1/2 overlap on each other, this is ensured. The technique is robust and shown to yield velocity fields of thin, previously immeasurable, vortical regions.

The second difficulty that arises in these measurements is due to the oscillating and deforming air-water interface—it is mirror-like (i.e. specular) and problematic—it causes very noisy data. The specular interface makes

surface detection in the images difficult. An experimental setup that utilizes the Brewster angle is adopted and the specular effects of the free-surface are reduced dramatically. It proved to be very effective.

The relatively small number of image pixels provided by the system is insufficient for extracting a dense array of velocity vectors; hence, special processing is necessary. Particle images acquired at several locations are analyzed using the PIV correlation method, and the estimated velocity fields are merged (with an overlap of 1/3 the image width) to provide coverage over an entire wavelength. Thus, wave generation repeatability and precise re-location of the imaging system are imperative. The imaging system and laser optics are mounted on a carriage astride a positional horizontal precision rail. The repeatability is examined by replication of the wave elevation profile measurements (Perlin *et al.*¹⁰). The results show that the deviations in the wave profiles are less than the pixel-resolution of the PIV system, as long as all the equipment (wave maker, laser light chopping mechanism, imaging system, etc.) is driven by the same set of electronic signals. Thus, the data-merging technique is shown to be accurate and effective.

A second recording/processing technique with double exposures of photographic film obtains high-resolution, high-accuracy PIV data. A different setup is used. The optical sensor plane of the digital imaging system is replaced by a 4 by 5 inch Kodak T-Max 400 film, and the laser beam is deflected by an acousto-optic modulator (AOM). The AOM acts as an on-off switch for the continuous Argon-Ion laser. The illumination duration is less than 500 μ sec (for each exposure) and the time interval between laser pulses and hence exposures is 4 msec. The digital imager trigger signal controls the AOM. A scanning mirror with feedback is added to the imaging optics, and the oscillation of the mirror is synchronized by the wavemaker driving signal with eight times the primary frequency. The amplitude is adjusted according to the feedback signal to provide a sufficient bias velocity for double-exposure PIV (Adrian¹⁵). This technique proved less effective in surface detection for one primary reason. The upper-most particle images for each single exposure are assumed to represent the water surface. Since the wave's forward (backward) face at the first (second) exposure is overlapped with the near surface region at the second (first) exposure, a sufficiently accurate wave profile is difficult to obtain. Therefore, the data acquired by this (double-exposure photographic film) method are used only to compare to the data recorded by the digital imaging system in the upper region close to the surface. It also provides the lower region data where the digital imaging system results are absent.

III. THE EXPERIMENTS

Three sets of experiments are conducted with different wavemaker frequencies: 4.21 Hz, 5.26 Hz, and 6.70 Hz; the associated wavelengths are approximately 100 mm, 70 mm, and 50 mm, respectively. Each set includes three forcing amplitudes. The wave maker is driven by a sinusoidal signal, and its motion is examined for repeatability. The displacement of the wavemaker matches the primary frequency input signal, while other (harmonic) frequency components show an amplitude less than 0.5% of the primary frequency component. Hence, the wave maker motion is essentially sinusoidal. The capillary ripples or other high-frequency components are present in the wave form due to resonance. They are not due to the presence of higher harmonics in the drive signal. The waves investigated are of moderate steepness ($ka = 0.130$ through 0.225) to maintain two-dimensionality and avoid modulation. The profiles show (almost) phase-locked underlying (primary) waves and ripples. The amplitudes of the primary waves and capillary ripples decrease monotonically in space due to viscous damping; however, their decrease is relatively slow compared to the time scale of the PIV image recording. Hence, the waves are quasi-steady in this steepness range.

Only the 5.26 Hz experiments are presented. These experiments are conducted with three different steepnesses: $ka = 0.225$, 0.200 , and 0.170 with wavelengths 70.0 mm, 67.0 mm, and 64.1 mm, respectively. The vorticity distribution is presented in Fig. 1. Waves of this frequency show seven parasitic capillary ripples along the forward surface of the underlying gravity waves. The $ka = 0.225$ waves shown in Fig. 1 (c) exhibit vorticity greater than 30 rad/sec in three troughs on the forward face, on the second, third, and fourth troughs (as shown by arrows in the figure) from the primary crest. A much weaker clockwise vortex is present in the first trough. The first two of these strong clockwise vortices are accompanied by adjacent upstream counter-clockwise counterparts. For the two lower steepness waves ($ka = 0.200$ and 0.170), strong vortices are not found; here, only one location has vorticity stronger than 10 rad/sec and it is located in the first trough of the steeper wave. Since there is less accuracy in the *wave-form* detection using PIV images, the profiles shown do not exhibit the finer details of those acquired by the vertically magnified images in Jiang *et al.*;¹¹ hence, Fig. 2 is included. This figure presents vertically exaggerated surface-elevation profiles for 5.26 Hz waves with about the same steepnesses as those presented in Fig. 1. Evidently, the parasitic capillary waves decayed rapidly as they travelled downstream. About 14 capillaries are seen in the uppermost profile including seven on the rear-facing side of the primary wave. As viscous damping removes energy from the wave train, the number and steepness of the parasitic waves decreases. In the second profile, about 10 parasitic waves are visible, while in the middle profile this number is reduced to about seven. In the farthest downstream profile, the capillaries are barely visible.

IV. DISCUSSION AND CONCLUDING REMARKS

For the 5.26 Hz waves, the wavelength is approximately 70 mm, and the wave profile clearly shows that

capillary ripple amplitudes decay spatially along the forward face of the underlying waves. For the $ka = 0.225$ waves, strong clockwise vortices appear at least in the second, third, and fourth troughs, while the accompanying counter-clockwise vortices in the crests of the capillary ripples are much weaker or absent in one case. Quantitative comparison of the magnitude is difficult since the experimental wave steepness of the capillary ripples cannot be measured accurately. And unlike the numerical simulation or theoretical prediction, the exact vorticity on the surface is unavailable (unless inadvisable extrapolation is used).

In the vorticity fields presented, and the numerical results by Mui and Dommermuth, the “capillary roller” predicted by the theory does not exist. However, similar phenomena are seen in certain experimental situations. The vorticity data presented here have moderate ka values. For higher energy waves (larger wavemaker stroke), the wave profiles become very unsteady, and an entire wavelength vorticity measurement cannot be made with the present equipment. However, by tracking particles captured in the crest area, with $ka = 0.250$ or higher, a jet-like flow immediately in front of the primary crests *is* found. That is, a small group of waterborne particles seems to travel at about the phase speed, much faster than the particles immediately beneath them. When such a flow is present, the wave profile is neither steady nor stable in any sense, and a turbulent flow field is observed in this area. Also, the wave profile has a decay rate faster than the well-known rate, $\partial a / \partial t = -2vk^2 a$.

For the first time, the velocity and vorticity fields beneath progressive gravity-capillary waves with parasitic ripples present are reported. Two new experimental techniques especially developed to facilitate these measurements are discussed briefly. The theoretical prediction, numerical simulation, and experimental investigation all show strong vortices at the capillary troughs. However, the capillary roller in the primary crest is not realized by the numerical simulation, and the experimental observation has difficulty generating temporally periodic waves with the required steepness. On the other hand, a capillary roller is observed qualitatively and reported by several researchers, especially for wind waves, but a careful flow field study (analytically or experimentally) is not available. In general, the vorticity magnitudes in the troughs of the parasitic capillaries are greater than those in the crests, in agreement with theory and numerical prediction. According to our laboratory observation with a mechanically generated wave train, the (spatial) amplitude decay seems to play an important role in the occurrence of capillary rollers. The decay rate is faster than the theoretical prediction presumably due to the unavoidable turbulence that occurs. Such a flow situation requires an experimental technique that can handle unsteady, very fine-scale eddies (turbulence) in a very thin near-surface region. The present effort demonstrates an effective approach utilizing the Brewster angle and the sub-pattern PIV technique.

ACKNOWLEDGMENTS

This research was supported by the Office of Naval Research under the University Research Initiative Ocean Surface Processes and Remote Sensing at the University of Michigan, Contract No. N00014-92-J-1650.

¹M.S. Longuet-Higgins, “The generation of capillary waves by steep gravity waves,” *J. Fluid Mech.*, **16**, 238-259 (1963).

²G.D. Crapper, “Non-linear capillary waves generated by steep gravity waves,” *J. Fluid Mech.*, **40**, 149-159 (1970).

³K.D. Ruvinsky and G.I. Freidman, “On the generation of capillary-gravity waves by steep gravity waves,” *Izv. Atmos. Ocean. Phys.*, **17**, 548-553 (1981).

⁴K.D. Ruvinsky, F.I. Feldstein, and G.I. Freidman, “Numerical simulations of the quasi-stationary stage of ripple excitation by steep gravity-capillary waves,” *J. Fluid Mech.*, **230**, 339-353 (1991).

⁵K. Okuda, S. Kawai, and Y. Toba, “Measurement of skin friction distribution along the surface of wind waves,” *J. Ocean. Soc. Japan*, **33**, 190-198 (1977).

⁶N. Ebuchi, H. Kawamura, and Y. Toba, “Fine structure of laboratory wind-wave surfaces studied using an optical method,” *Boundary-Layer Met.*, **39**, 133-151 (1987).

⁷M.S. Longuet-Higgins, “Capillary rollers and bores,” *J. Fluid Mech.*, **240**, 659-679 (1992).

⁸R.C.Y. Mui and D.G. Dommermuth, “The vortical structure of parasitic capillary waves,” *J. Fluid Engr.*, **117**, 355-361 (1995).

⁹J.C. Lin and D. Rockwell, “Evolution of a Quasi-steady breaking wave,” *J. Fluid Mech.*, **302**, 29-44 (1995).

¹⁰M. Perlin, H. Lin, and C.-L. Ting, “On parasitic capillary waves generated by steep gravity waves: an experimental investigation with spatial and temporal measurements,” *J. Fluid Mech.*, **255**, 597-620 (1993).

¹¹L. Jiang, H.J. Lin, W.W. Schultz, and M. Perlin, “Unsteady ripple generation on steep gravity-capillary waves,” *J. Fluid Mech.*, **386**, 281-304 (1999).

¹²H.J. Lin and M. Perlin, “Improved methods for thin, boundary layer investigations,” *Exp. Fluids*, **25**, 431-444 (1998).

¹³R.D. Keane, R.J. Adrian, and Y. Zhang, “Super-resolution particle imaging velocimetry,” *Meas. Sci. Tech.*, **6**, 754-768 (1995).

¹⁴H.T. Huang, H.E. Fiedler, and J.J. Wang, “Limitation and improvement of PIV. Part II: Particle image distortion, a novel technique,” *Exp. Fluids*, **15**, 263-273 (1993).

¹⁵R.J. Adrian, “Particle-imaging techniques for experimental fluid mechanics,” *Ann. Rev. Fluid Mech.*, **23**, 261-304 (1991).

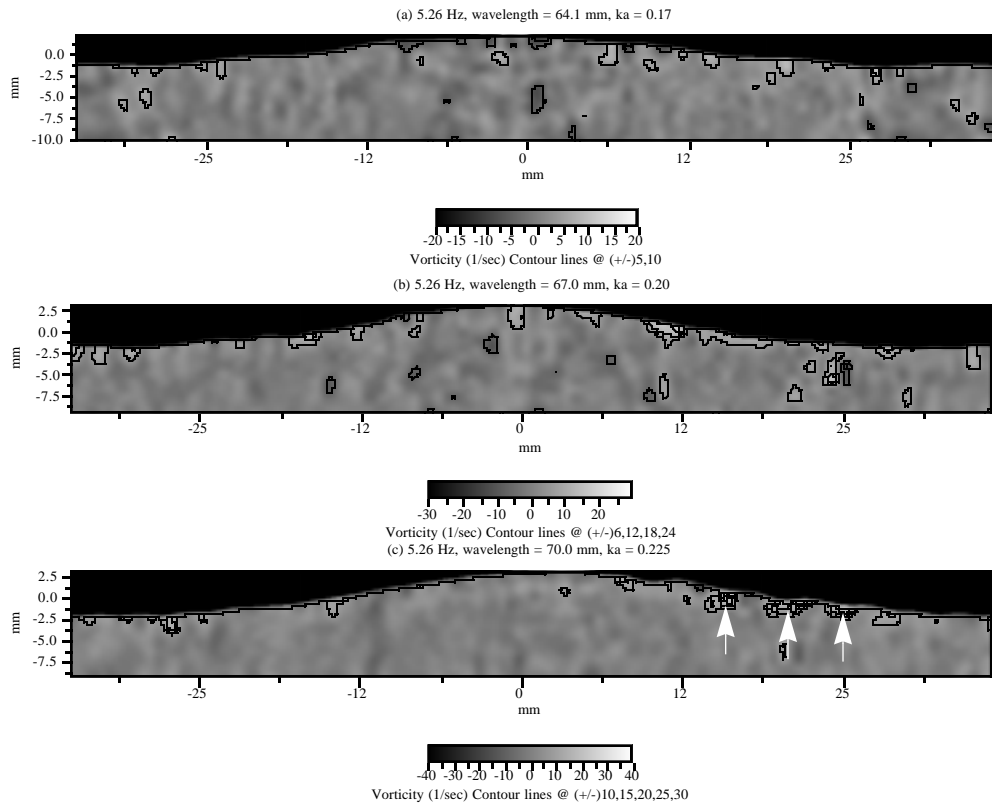


Fig. 1. Vorticity distributions beneath 5.26 Hz gravity-capillary waves with steepnesses, ka , (a) 0.17, (b) 0.20, and (c) 0.225. Axes are in mm. The arrows in the lower figure locate the second, third, and fourth capillary troughs discussed in the text.

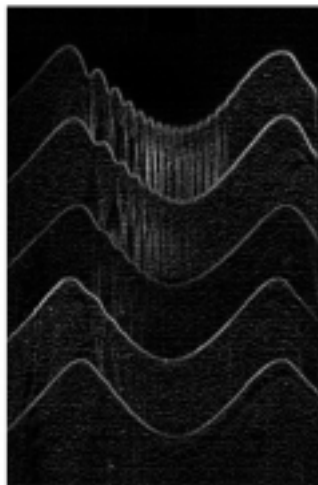


Fig. 2. Surface elevation profiles of 5.26 Hz waves measured, in 30 mm intervals, 180 mm (uppermost profile) through 300 mm (lowermost profile) downstream of the wave maker. The wave steepnesses are 0.21 through 0.17, approximately the same range of steepnesses as the waves/vorticity fields shown in Fig. 1. A cylindrical lens system is used to generate the vertical exaggeration of about 5.8 in these images.